Disturbance of the Sm-Nd isotopic system by metasomatic alteration: A case study of fluorapatite from the Sin Quyen Cu-LREE-Au deposit, Vietnam

Xiao-Chun Li[1,*], Mei-Fu Zhou[1,*], Yue-Heng Yang[2], Xin-Fu Zhao[3], and Jian-Feng Gao[4]

[1]Department of Earth Sciences, The University of Hong Kong, Hong Kong SAR, China
[2]State Key Laboratory of Lithospheric Evolution, Institute of Geology and Geophysics, Chinese Academy of Sciences, Beijing, China
[3]State Key Laboratory of Geological Processes and Mineral Resources, and Faculty of Earth Resources, China University of Geosciences, Wuhan 430074, China
[4]State Key Laboratory of Ore Deposit Geochemistry, Institute of Geochemistry, Chinese Academy of Sciences, Guiyang 550002, China

Abstract

The Neoproterozoic (840 Ma) Sin Quyen deposit in northwestern Vietnam contains replacement Cu-LREE-Au orebodies in Proterozoic metasedimentary rocks. In this deposit, LREE-bearing minerals include allanite-(Ce), monazite-(Ce), chevkinite-(Ce), and fluorapatite. Fluorapatite from orebodies has undergone variable degrees of metasomatic alteration. Samarium-neodymium isotopic analyses were conducted on altered fluorapatite, and also on allanite-(Ce) and monazite-(Ce), to investigate whether such metasomatism can affect the Sm-Nd isotope system.

Allanite-(Ce) and monazite-(Ce) have $^{147}Sm/^{144}Nd$ ratios ranging from 0.0359 to 0.0549, and $^{143}Nd/^{144}Nd$ ratios from 0.51147 to 0.51172. Their initial $^{143}Nd/^{144}Nd$ values at the time of mineralization range from 0.51126 to 0.51148, but mostly cluster between 0.51135 and 0.51145. Thus, the primary ore-forming fluids were relatively homogeneous in their Sm-Nd isotopic compositions. In the $^{147}Sm/^{144}Nd$ vs. $^{143}Nd/^{144}Nd$ diagram, the compositions of allanite-(Ce) and monazite-(Ce) generally plot along a Sm-Nd isochron of 840 Ma, implying that the Sm-Nd isotopic systems of these minerals were either closed or only slightly modified. In contrast, altered fluorapatite crystals have $^{147}Sm/^{144}Nd$ ratios varying from 0.0667 to 0.1348, and $^{143}Nd/^{144}Nd$ ratios from 0.51160 to 0.51199. The calculated initial $^{143}Nd/^{144}Nd$ ratios range widely from 0.51114 to 0.51141, with most values lower than those of the allanite-(Ce) and monazite-(Ce). In the $^{147}Sm/^{144}Nd$ vs. $^{143}Nd/^{144}Nd$ diagram, their compositions mostly plot below the 840-Ma Sm-Nd isochron. Petrographic observations and trace elemental analyses show that metasomatic modification of fluorapatite grains led to increases of their Sm/Nd ratios. The unaltered domains in the grains have Sm/Nd ratios varying from 0.114 to 0.200, with an average value of 0.161; whereas the altered domains have Sm/Nd ratios varying from 0.111 to 0.254, with an average value of 0.183. The increased Sm/Nd ratios can cause the calculated initial $^{143}Nd/^{144}Nd$ ratios to be lower than actual initial isotopic ratios, and can also result in compositional deviations from the reference Sm-Nd isochron.

This study demonstrates that the traditionally assumed inert Sm-Nd isotopic system can be metasomatically disturbed due to changes in the Sm/Nd ratio. Therefore, care must be taken when interpreting the Sm-Nd isotopic data from apatite/apatite-rich rocks that have undergone metasomatic alteration.

Keywords: Apatite, metasomatic alteration, Sm-Nd isotopes

Introduction

Apatite is a common accessory mineral in igneous, metamorphic, and sedimentary rocks, and hydrothermal ore deposits. Its mineral structure can accommodate a range of trace elements, such as halogens, S, V, As, Sr, and rare earth elements (REE) (Hughes and Rakovan 2015), which are sensitive to diverse geological processes. Thus, apatite has gained considerable attention as a mineral with many uses within the Earth sciences. However, this mineral is susceptible to fluid-induced alteration over a wide range of pressures and temperatures (Harlov 2015 and references therein), raising questions about the interpretation of its elemental

and isotopic composition.

Apatite commonly contains moderate to high concentrations of Sm and Nd. Advances in analytical techniques make it possible to determine the Sm-Nd isotopes of apatite, on a sub-grain scale, by laser ablation multi-collector inductively coupled plasma-mass spectrometry (e.g., Fisher et al. 2011; Yang et al. 2014). This approach can provide rapid, texturally sensitive isotopic data, which has many advantages over previous bulk-rock analyses. For example, it allows assessment of Nd isotope equilibrium/disequilibrium among minerals of high-grade metamorphic rocks. Such data are important for understanding Nd isotope exchange during both metamorphism and crustal anatexis processes (Hammerli et al. 2014). Moreover, in situ Sm-Nd isotopic analysis of apatite is important to determine the primary isotopic signature of mantle-

* E-mail: lixiaochun86@gmail.com and mfzhou@hku.hk

derived rocks by analyzing the composition of apatite that directly crystallized from the initial unaffected magmas (Wu et al. 2011, 2013). Apatite is also useful for sediment provenance studies based on its initial Nd isotope composition. Such studies can help unravel the tectonic history of the hinterland and provide insights into the origins and transport pathways of the sediments (e.g., Foster and Carter 2007; Henderson et al. 2010). It is also notable that apatite is one of the major hosts of Sm and Nd in many rocks, such as peraluminous and metaluminous granites (Bea 1996), carbonatites (Chakhmouradian et al. 2017), high-grade metamorphic rocks (Harlov and Förster 2002; Janots et al. 2018), and Kiruna-/IOCG-type hydrothermal deposits (Harlov et al. 2002; Schoneveld et al. 2015). This means that the Sm-Nd isotopic composition of apatite can partially or even largely control that of the host rocks. Given the significance of the Sm-Nd isotopic system in apatite, it is necessary to have a proper understanding of the metasomatic effects on the Sm-Nd isotopic changes in any study of apatite. However, to our knowledge, there are only sparse studies concerning this issue.

REE-rich fluorapatite crystals are widespread in the IOCG-type Sin Quyen deposit, northwestern Vietnam, and many crystals have been altered during post-ore metasomatic processes. The altered fluorapatite crystals may record Sm-Nd isotopic changes, and thus provide a good opportunity to study metasomatism-induced isotopic disturbance. In this paper, we present petrographic, elemental, and in situ and bulk-mineral Sm-Nd isotopic data for altered fluorapatite from the Sin Quyen deposit. For comparison, in situ Sm-Nd isotopic data for allanite-(Ce) and monazite-(Ce) from orebodies were also obtained. The comprehensive data set shows that the Sm-Nd isotopic system of fluorapatite could be variably disturbed during metasomatism, indicating that care must be taken when using Sm-Nd isotopes of altered apatite as geological indicators.

DEPOSIT GEOLOGY

The Sin Quyen deposit is hosted in a metamorphic complex in northwestern Vietnam (Fig. 1a). The protoliths of the metamorphic complex include Archean to Paleoproterozoic igneous intrusions and Paleoproterozoic to Neoproterozoic sedimentary rocks, all of which have been metamorphosed up to amphibolite facies. The metamorphic complex was intruded by Neoproterozoic to Mesozoic plutons, and unconformably covered by Cambrian to Triassic sedimentary rocks (Fig. 1a). Orebodies in the Sin Quyen deposit are distributed along a NW-SE trending zone, about 2.5 km long and 200 to 400 m wide (Fig. 1b). The mining area is divided into the eastern and western mining districts by the Ngoi Phat River. Exploration in the 1990s showed that this deposit contains 52.8 Mt ore at 0.91 wt% Cu, 0.7 wt% light REE (LREE), and 0.44 g/t Au (McLean 2001).

In this deposit, orebodies are hosted mainly in gneiss and mica-schist. The protoliths of ore-hosting rocks were Neoproterozoic sedimentary rocks (<920 Ma) (Li et al. 2018b). Individual orebodies are lenses 50 to 600 m long, and 5 to 100 m wide, which extend 50 to 400 m vertically. In a plan view, the orebodies have an overall NW-SE strike, and are generally S-shaped. In cross
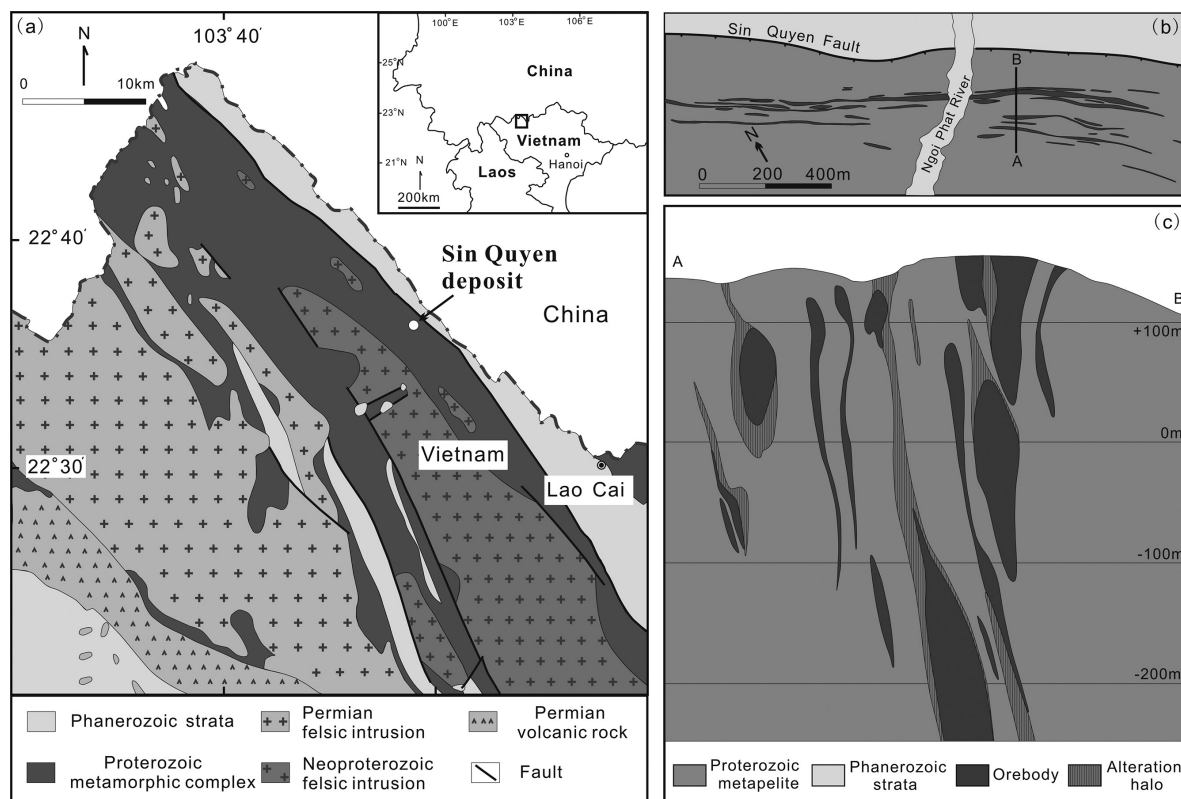

FIGURE 1. (a) Geological map of the northwestern Vietnam region. **(b)** Simplified geological map of the Sin Quyen deposit (modified from Ta et al. 1975). **(c)** Cross section A-B located in **a**, showing the distribution of orebodies (modified from McLean 2001).
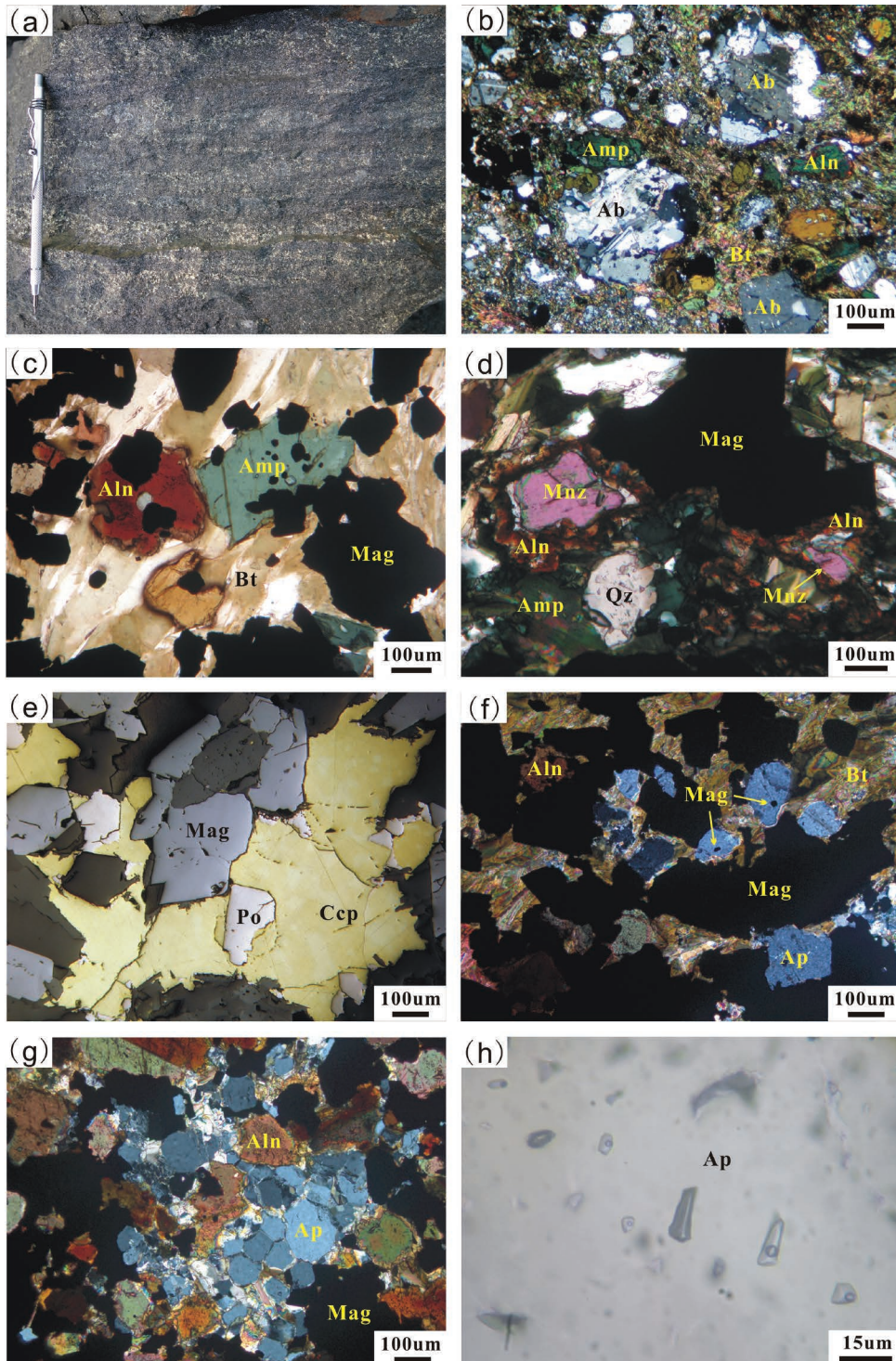
FIGURE 2. (a) A sample of banded ore, which mainly contains magnetite- and chalcopyrite-rich bands. (b) Stage I albite crystals overprinted by later-stage amphibole and biotite. (c) Typical mineral assemblage of stage II [magnetite + allanite-(Ce) + amphibole + biotite]. (d) Monazite-(Ce) crystals in ore sample. (e) Stage III sulfide minerals overprinting earlier stage minerals. (f) Individual fluorapatite crystals in contact with magnetite, and biotite. (g) Fluorapatite aggregates in contact with allanite-(Ce) and magnetite. (h) Two-phase fluid inclusions in fluorapatite. Mineral abbreviations: Aln = allanite-(Ce), Amp = amphibole, Ap = fluorapatite, Bt = biotite, Ccp = chalcopyrite, Mag = magnetite, Mnz = monazite-(Ce), Po = pyrrhotite, Qz = quartz. (Color online.)

sections, they dip at high angles to the northeast or, locally, to the southwest (Fig. 1c). The orebodies consist mainly of massive or banded replacement ores (Fig. 2a), which have experienced variable degrees of post-ore deformation. However, the main ore mineral assemblages and textures have been well preserved.

Three principle stages of alteration and mineralization have been identified in the Sin Quyen deposit: (I) pre-ore Na alteration; (II) Ca-K alteration and associated Fe-LREE mineralization; and (III) Cu-Au mineralization. Stage I Na alteration is recorded by the formation of hydrothermal albite in orebodies and ore-hosting rocks (Fig. 2b). Minor amounts of magnetite, monazite-(Ce), and chevkinite-(Ce) can also be identified in this stage. Stage II Ca-K

TABLE 1. A list of fluorapatite-bearing samples

Sample no.	Locality	Rock type	Mineralogy
SQ13-96	North border of the western mining district	Massive ore sample	Stage I: Ab±Mag
			Stage II: Mag+Aln+Amp+Ap
			Stage III: Ccp+Bt±Py
SQ13-110	North border of the western mining district	Banded ore sample	Stage I: Ab+Chev+Mnz
			Stage II: Aln+Ap
			Stage III: Bt±Ccp
LC11-55	Ore pile in the eastern mining district	Banded ore sample	Stage II: Mag+Amp+Aln+Bt+Ap
			Stage III: Ccp
LC11-77	Ore pile in the eastern mining district	Massive ore sample	Stage II: Mag+Aln+Bt+Amp+Ap
			Stage III: Ccp+Po

alteration is characterized by the formation of amphibole and biotite, accompanied by lesser amounts of clinopyroxene, garnet, and titanite. The associated Fe mineralization is represented by abundant magnetite. The LREE mineralization is characterized by abundant allanite-(Ce) and subordinate LREE-rich fluorapatite, monazite-(Ce), and chevkinite-(Ce) (Figs. 2c and 2d). Stage III Cu-Au mineralization is characterized by deposition of sulfide minerals, mainly chalcopyrite and pyrrhotite, accompanied by subordinate pyrite and gold-bearing phases (Fig. 2e).

Geochronological studies demonstrate that the main mineralization event occurred at ca. 840 Ma (Li et al. 2018b). The orebodies were subsequently intruded by many Neoproterozoic (736–758 Ma) granitic dikes/stocks (Fig. 1c, Li et al. 2018a), and experienced an extensive metamorphic overprint at ca. 30 Ma (Li et al. 2018b). On the basis of alteration mineralogy and isotopic compositions, it was proposed that the mineralization was genetically associated with Neoproterozoic subduction-related magmatic activity (Li et al. 2018b).

SAMPLING AND ANALYTICAL METHODS

Fluorapatite is widespread in the orebodies but varies in abundance from <1% to >10%. In this study, four ore samples that contain >5 vol% apatite were selected for study. Two samples, SQ13-96 and SQ13-110, were collected from two separate orebodies in the western mining district, and the remaining two samples (LC11-55 and LC11-77) were from ore stockpiles of the eastern mining district. The main features of the studied samples are listed in Table 1.

Polished thin sections of each sample were investigated first by petrographic microscopy, and then backscattered electron (BSE) images were obtained using a JEOL JXA-8230 electron microprobe at The University of Hong Kong. Major element compositions of fluorapatite were determined using the same microprobe, following the analytical procedure described by Goldoff et al. (2012). The accelerating voltage was set at 15 kV, the beam current at 20 nA, and the beam diameter at 10 μm. The analyzing crystals were PET (S, P, Ca, Sr, and Cl), LiF (Ce, Fe, and Mn), LDE1 (F), and TAP (As, Si, and Na). The $K\alpha$ line was chosen for the analyses of S, P, Si, Fe, Mn, Ca, Na, F, and Cl; and the $L\alpha$ line for As, Ce, and Sr. The counting times on peaks were 10 s for F, Cl, Na, and K; and 20 to 40 s for other elements. Background intensities were measured on both sides of the peak for half of the peak time. The standards were lazurite for S and Sr; apatite for P, Ca, and F; gallium arsenide for As; albite for Si and Na; monazite for Ce; magnetite for Fe; rhodonite for Mn; and tugtupite for Cl. All data were corrected using standard ZAF correction procedures. The EMPA data are presented in Supplemental[1] Table 1.

Trace element analyses of fluorapatite were performed using a Geolas Pro 193 nm laser ablation (LA) system coupled to an Agilent Technologies 7900 type inductively coupled plasma-mass spectrometer (ICP-MS) at the Institute of Geochemistry, Chinese Academy of Sciences. The analyses were performed on thin sections, with a beam diameter of 32 μm and a repetition rate of 4 Hz. The counting times were ~20 s for the background analyses, and ~50 s for the sample analyses. The glass standard NIST 610 was used for external calibration and was analyzed twice after eight sample analyses. Calcium was used as the internal standard, and the content of CaO was determined by EMP analyses. The apatite standard Durango was measured as an external standard to monitor the analytical accuracy. Data reduction was performed by the software ICPMSDataCal. The LA-ICP-MS trace element data are listed in Supplemental[1] Table 2.

In situ Sm-Nd isotopic analyses were performed using a Neptune multi-collector

(MC) ICP-MS, equipped with a Geolas 193 nm excimer laser ablation system at the Institute of Geology and Geophysics, Chinese Academy of Sciences (IGGCAS). The analyses were conducted on thin sections, with a spot size of 90 or 110 μm and a repetition rate of 8 Hz for fluorapatite, a spot size of 20 μm, and a repetition rate of 4 Hz for monazite-(Ce); and a spot size of 32 μm and a repetition rate of 6 Hz for allanite-(Ce). Each spot analysis involved ~20 s of background data acquisition and ~50 s of data acquisition from the sample. After analyses of eight samples, two standards were analyzed for external calibration. The apatite standard Ap 1 was used for the analyses of fluorapatite (reference values: $^{147}Sm/^{144}Nd = 0.0822 \pm 0.0014$, $^{143}Nd/^{144}Nd = 0.511349 \pm 0.000038$; Yang et al. 2014), and the monazite standard Namaqua was used for the analyses of monazite-(Ce)/allanite-(Ce) (reference values: $^{147}Sm/^{144}Nd = 0.0977 \pm 0.0002$, $^{143}Nd/^{144}Nd = 0.511896 \pm 0.000032$; Liu et al. 2012). The isobaric interference of ^{144}Sm on ^{144}Nd is significant. To correct for this interference, we have used the $^{147}Sm/^{149}Sm$ ratio (1.08680) and the measured $^{147}Sm/^{149}Sm$ ratio to calculate the Sm fractionation factor, and then used the measured ^{147}Sm intensity and the natural $^{147}Sm/^{144}Sm$ ratio to estimate the Sm interference on mass 144. The interference-corrected $^{146}Nd/^{144}Nd$ ratio was then normalized to 0.7219 to calculate the Nd fractionation factor. Finally, the $^{143}Nd/^{144}Nd$ and $^{145}Nd/^{144}Nd$ ratios were normalized using the exponential law. The $^{147}Sm/^{144}Nd$ ratio was calculated using the exponential law after correcting for the isobaric interference of ^{144}Sm on ^{144}Nd as described above, and then was externally calibrated against the $^{147}Sm/^{144}Nd$ ratio of the standards. The raw data were exported offline and the whole data-reduction procedure was performed using an in-house Excel Visual Basic for Applications (VBA) macro program. The apatite standard Ap 2 was measured to monitor the analytical accuracy for apatite, yielding weighted mean $^{147}Sm/^{144}Nd$ and $^{143}Nd/^{144}Nd$ ratios of 0.0755 ± 0.0008 and 0.511034 ± 0.000037, respectively, which are consistent, within uncertainty, with the reported values of 0.0764 ± 0.0002 and 0.511007 ± 0.000030, respectively (Yang et al. 2014). The in-situ Sm-Nd isotopic data are listed in Supplemental[1] Table 3.

Bulk-mineral Sm-Nd isotopic compositions of fluorapatite were analyzed at IGGCAS. Fluorapatite crystals were separated from crushed samples using a conventional density separation technique. About 100 mg of fluorapatite was weighed into a 7 mL "Savillex" polytetrafluoroethylene beaker, and the appropriate amount of mixed ^{149}Sm-^{150}Nd spike was added. Samples were dissolved in distilled HF + HNO_3 + HBO_3. Chemical separation was performed using a two-stage ion exchange procedure. First, REE were isolated from the matrix elements using a standard cation exchange resin. After that, Sm and Nd were separated using Eichrom LN (LN-C-50B, 100 to 150 μm, 2 mL) chromatographic columns. The Sm-Nd isotopic measurements were conducted using an IsoProbe-T thermal ionization mass spectrometer. The reference material BCR-2 was measured to monitor the accuracy of the entire analytical procedure, with the following results: 6.67 ppm Sm, 28.56 ppm Nd, and $^{143}Nd/^{144}Nd = 0.512651 \pm 16$ (2σ), which are comparable to the reported reference values (Sm = 6.547 ppm, Nd = 28.26 ppm, $^{143}Nd/^{144}Nd = 0.512635 \pm 29$; Jochum et al. 2005). The bulk-mineral Sm-Nd isotopic data are listed in Supplemental[1] Table 4.

FLUORAPATITE PETROGRAPHY

Fluorapatite occurs as single crystals or aggregates in contact with magnetite, allanite-(Ce), amphibole, biotite, and/or garnet of stage II (Figs. 2f and 2g). Some fluorapatite crystals contain inclusions of magnetite and biotite. Individual fluorapatite crystals are subhedral to anhedral in shape and have lengths ranging from 50 to 150 μm. Many grains contain intra-crystal fractures, and some have two-phase fluid inclusions (Fig. 2h). The fluid inclusions are commonly distributed along lines, so they are interpreted to have been trapped after crystallization of fluorapatite.

In BSE images, we recognize five textural types of fluorapatite. Type I grains show very faint or concentric growth zoning (Figs.

3a and 3b). Type II varieties have irregular BSE-bright cores surrounded by darker rims (Fig. 3c). The BSE-dark rims can be either continuous or discontinuous and have variable thicknesses. Boundaries between the BSE-dark and BSE-bright areas may be smooth or irregular. The BSE-bright areas are not homogeneous: some show slightly different levels of gray and some contain small BSE-dark patches. Type III crystals have not only BSE-dark areas along rims but also irregular BSE-dark veins passing through the bright interiors (Fig. 3d). Type IV crystals have a small BSE-bright core or some isolated BSE-bright patches surrounded by relatively wide dark areas (Fig. 3e). These grains grade into homogeneous and relatively dark crystals of Type V (Fig. 3f).

FLUORAPATITE MINERAL COMPOSITION

Major and trace elements

Fluorapatite crystals from the Sin Quyen deposit consist chiefly of CaO and P_2O_5, with 2.39 to 3.71 wt% F and 0.01 to 1.23 wt% OH (estimated via charge balance on the halogen site). They also contain minor SiO_2 (below detection limit to 1.01 wt%), Ce_2O_3 (below detection limit to 1.29 wt%), SrO (below detection limit to 0.22 wt%), and FeO (0.01 to 0.64 wt%). The BSE-bright domains generally have higher contents of Ce_2O_3 and SiO_2 than the BSE-dark domains. Some crystals contain detectable Na_2O (<0.05 wt%) and Cl (<0.02 wt%).

Different fluorapatite domains contain highly variable (REE+Y) concentrations (319 to 20388 ppm), which correlate positively with Si (Fig. 4a). Thus, the REE^{3+} ions are principally charge-balanced through the coupled substitution $Si^{4+} + (REE+Y)^{3+} = P^{5+} + Ca^{2+}$. It is proposed that in apatite the REE^{3+} ions can also be charge-balanced through the coupled substitution $Na^+ + (REE+Y)^{3+} = 2Ca^{2+}$ (Roeder et al. 1987; Pan and Fleet 2002). However, the correlation between (REE+Y) and Na is not obvious (Fig. 4b), which indicates that the latter coupled substitution is not important for the samples in this study. In each sample, the BSE-dark areas generally have lower (REE+Y) concentrations and higher Sm/Nd ratios than the bright areas (Figs. 5a to 5d). Trace element analyses were conducted on both BSE-bright and BSE-dark areas of eight fluorapatite crystals. In all crystals, the dark areas have lower (REE+Y) concentrations than the corresponding bright areas. In six of the crystals, the dark area has a higher Sm/Nd ratio than the corresponding bright area, whereas in one crystal, the dark and bright areas have similar Sm/Nd ratios, and in the other, the BSE-dark area has a lower Sm/Nd ratio than the BSE-bright area. Although the BSE-dark domains have lower REE concentrations than the BSE-bright domains, their chondrite-normalized REE patterns are similar, with nearly flat or slightly right-/left-inclined profiles from La to Pr, right-inclined profiles from Nd to Dy, and slightly left-inclined to nearly flat profiles from Ho to Lu (Figs. 5e to 5h). The BSE-dark domains also contain lower amounts of U (21.4 ppm on average), As (49.7 ppm on average), and Ge (9.29 ppm on average) than the BSE-bright domains (63.6 ppm U, 87.5 ppm As, and 24.5 ppm Ge on average).

Sm-Nd isotopes

In situ Sm-Nd isotopic compositions of fluorapatite were analyzed using large laser spots (90 or 110 μm), so most analyses include mixed BSE-bright and BSE-dark areas. Overall, the analyses yielded scattered $^{147}Sm/^{144}Nd$ (0.0667 to 0.1348) and $^{143}Nd/^{144}Nd$ ratios (0.51160 to 0.51199) (Fig. 6a). Spots containing higher proportions of BSE-bright domains generally have lower $^{147}Sm/^{144}Nd$ ratios than those with higher proportions of BSE-dark domains (Fig. 6a). Bulk-mineral Sm-Nd isotopic analyses of fluorapatite yielded more restricted $^{147}Sm/^{144}Nd$ (0.1024 to 0.1112) and $^{143}Nd/^{144}Nd$ ratios (0.511809 to 0.511822) (Table 2).

Compared with fluorapatite, monazite-(Ce) and allanite-(Ce) have relatively uniform isotopic compositions (Fig. 6a). Monazite-(Ce) has $^{147}Sm/^{144}Nd$ and $^{143}Nd/^{144}Nd$ ratios varying from 0.0375 to 0.0549, and from 0.51157 to 0.51172, respectively. Allanite-(Ce) has $^{147}Sm/^{144}Nd$ and $^{143}Nd/^{144}Nd$ ratios varying from 0.0359 to 0.0508, and from 0.51147 to 0.51170, respectively.

DISCUSSION

Interpretation of the fluorapatite textures

Most of the fluorapatite crystals, except for those of Type V, show compositional zoning. We note that the development of BSE-dark domains extend from grain rims deep into the interiors. The boundaries between BSE-bright and BSE-dark domains are commonly irregular. Some vein-like BSE-dark domains cut the bright domains. These features imply that fluids played an important role in the formation of the zoned crystals. Therefore, we suggest that the texturally different fluorapatite grains record different degrees of hydrothermal reactions.

Original unaltered REE-rich fluorapatite grains are homogeneous in composition or show primary growth zoning (Type I). During the early stages of alteration, the margins of the fluorapatite began to react with hydrothermal fluids, forming BSE-dark rims surrounding the BSE-bright cores (Type II). Penetration of the fluids into the interiors of fluorapatite formed the irregular BSE-dark veins (Type III). Further alteration led to the replacement of most of BSE-bright domains by the BSE-dark domains, leaving only small BSE-bright cores or isolated BSE-bright patches (Type IV). Finally, complete alteration resulted in the total replacement of BSE-bright fluorapatite by BSE-dark fluorapatite (Type V).

Disturbance of the Sm-Nd isotopic system by metasomatic alteration

Given that many fluorapatite crystals in the Sin Quyen deposit have experienced metasomatic alteration, monazite-(Ce) and allanite-(Ce) from this deposit may also have experienced similar alteration (Li and Zhou 2017). However, the alteration may not disturb the Sm-Nd isotopic systems of monazite-(Ce) and allanite-(Ce) to large extents, because both phases contain substantially high contents of Sm and Nd. Thus, the initial Sm-Nd isotopic compositions of monazite-(Ce) and allanite-(Ce) could be taken to represent those of the ore-forming fluids. We calculated the initial $^{143}Nd/^{144}Nd$ values of monazite-(Ce) and allanite-(Ce) at the time of mineralization (840 Ma), and found that they range from 0.51126 to 0.51148, mostly between 0.51135 and 0.51145 (Fig. 6b). Such results indicate that the ore-forming fluids of the Sin Quyen deposit had relatively homogeneous Nd isotopic compositions. Fluorapatite crystals that precipitated from the ore-forming fluids would be expected to have similarly
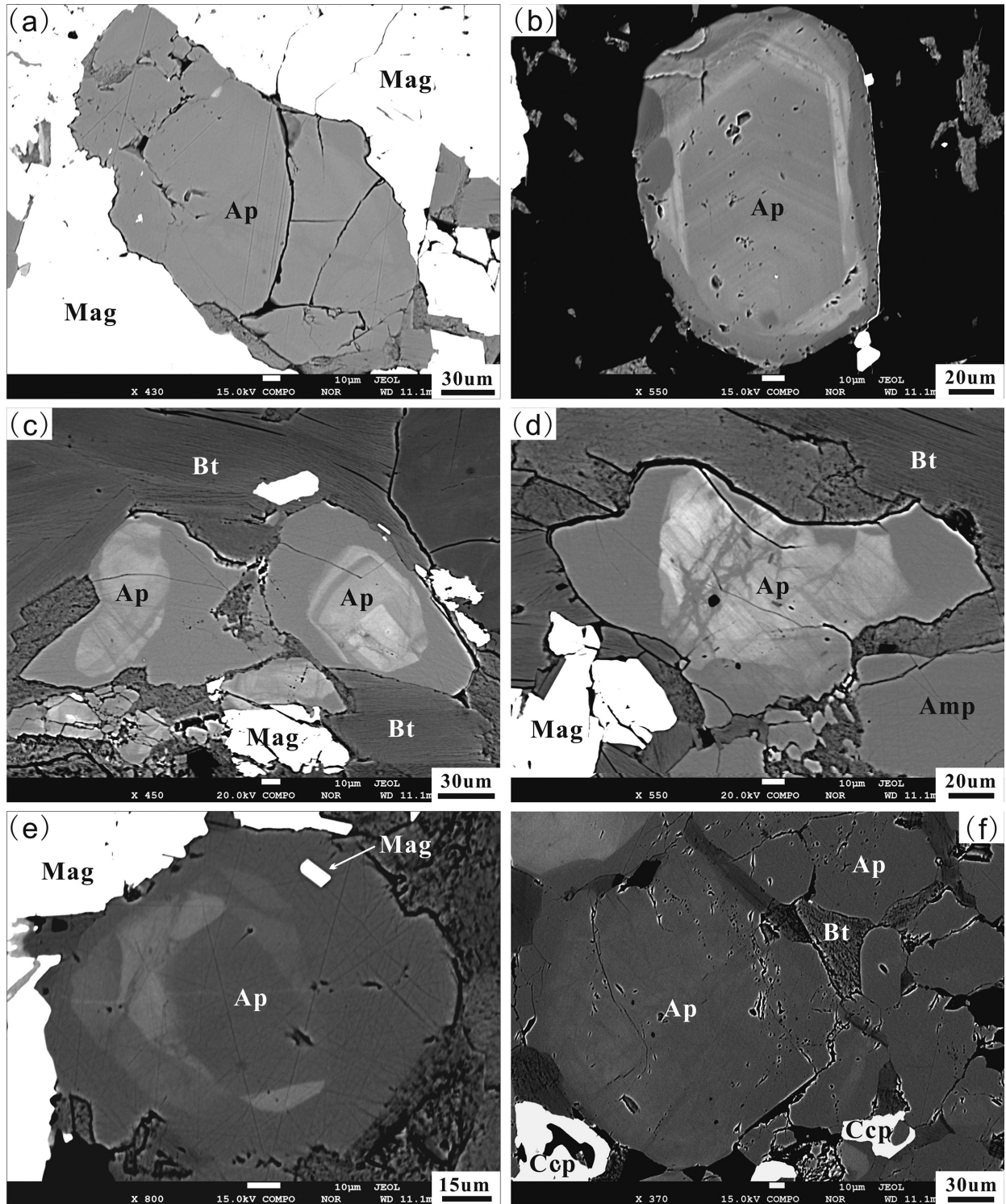
FIGURE 3. (**a**) A fluorapatite crystal with very faint zoning. (**b**) A fluorapatite crystal with concentric growth zoning. Note that this crystal has discontinuous dark areas along the grain rim. (**c**) Fluorapatite crystals with dark rims of varying thickness around the bright cores. (**d**) A fluorapatite crystal with dark veins crossing the bright interior. (**e**) A fluorapatite crystal with small bright patches surrounded by dark area. (**f**) Homogeneous, dark fluorapatite crystals. Mineral abbreviations are the same as those in Figure 2.

▶ **Figure 4.** Plots of Si vs. (REE+Y) and Na vs. (REE+Y) concentrations for fluorapatite.
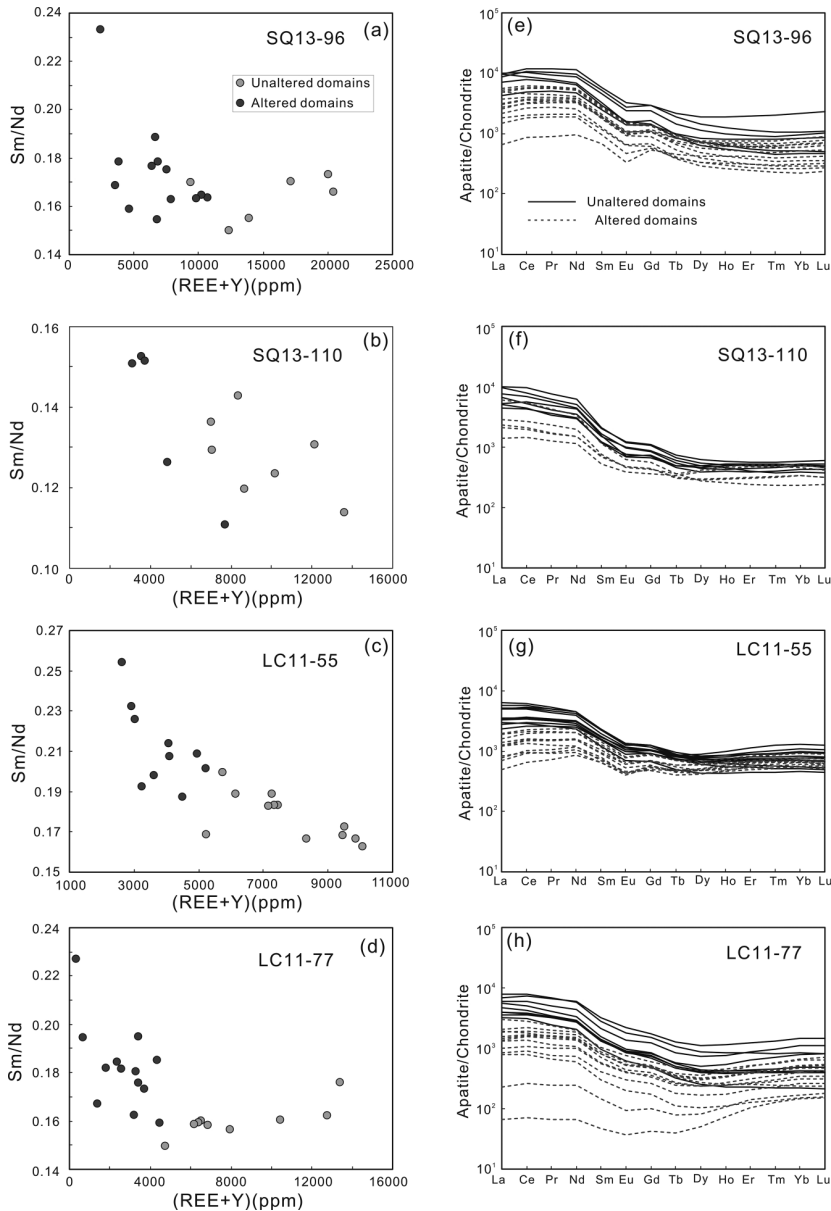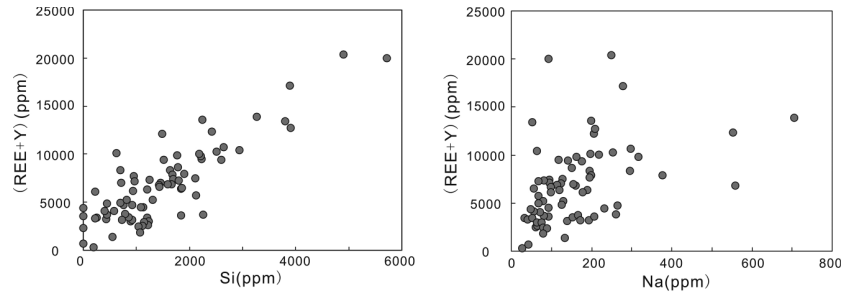
Figure 5. (**a** to **d**) Plots of (REE+Y) vs. Sm/Nd for fluorapatite from the samples in this study. (**e** to **h**) Chondrite-normalized REE profiles for fluorapatite from studied samples.

homogeneous Nd isotopic compositions. However, their initial $^{143}Nd/^{144}Nd$ values range widely from 0.51114 to 0.51141, mostly lower than those of monazite-(Ce) and allanite-(Ce) (Fig. 6c). Assuming an initial $^{143}Nd/^{144}Nd$ value of 0.51140 [the average initial $^{143}Nd/^{144}Nd$ value of monazite-(Ce) and allanite-(Ce)], a reference isochron with an age of 840 Ma is shown in the $^{147}Sm/^{144}Nd$ vs. $^{143}Nd/^{144}Nd$ diagram (Fig. 6a). In this diagram, the compositions of most analyzed fluorapatites, especially grains with higher proportions of BSE-dark (altered) domains, plot below the reference isochron (Fig. 6a), indicating that the Sm-Nd isotopic system was disturbed during the post-ore metasomatic process.

Disturbance of the Sm-Nd isotopic system could potentially be due to: (1) change(s) in the $^{143}Nd/^{144}Nd$ ratio, (2) change(s) in the $^{147}Sm/^{144}Nd$ ratio, or (3) a combination of reasons 1 and 2. If the metasomatic fluids had $^{143}Nd/^{144}Nd$ ratios different from those of unaltered fluorapatite, the $^{143}Nd/^{144}Nd$ ratios of fluorapatite could have been changed, because Nd can be introduced into fluorapatite from the fluids. However, it is difficult to determine how much Nd was gained from the metasomatic fluid. The accurate isotopic composition of metasomatic fluid is not known. Thus, it cannot be certain if the disturbance of Sm-Nd isotopic system was mainly due to the changes in the $^{143}Nd/^{144}Nd$ ratios. Variable removal of Nd from fluorapatite during metasomatism may imply an insignificant gain of Nd from the fluid. Thus, the $^{143}Nd/^{144}Nd$ ratio of fluorapatite may not be changed significantly.

Our analyses show that the Sm/Nd ratios of fluorapatite commonly increased during metasomatism, although in rare crystals the ratios decreased. If the Sm/Nd ratios were increased immediately after the formation of fluorapatite, the compositions of altered domains would evolve along new paths, but
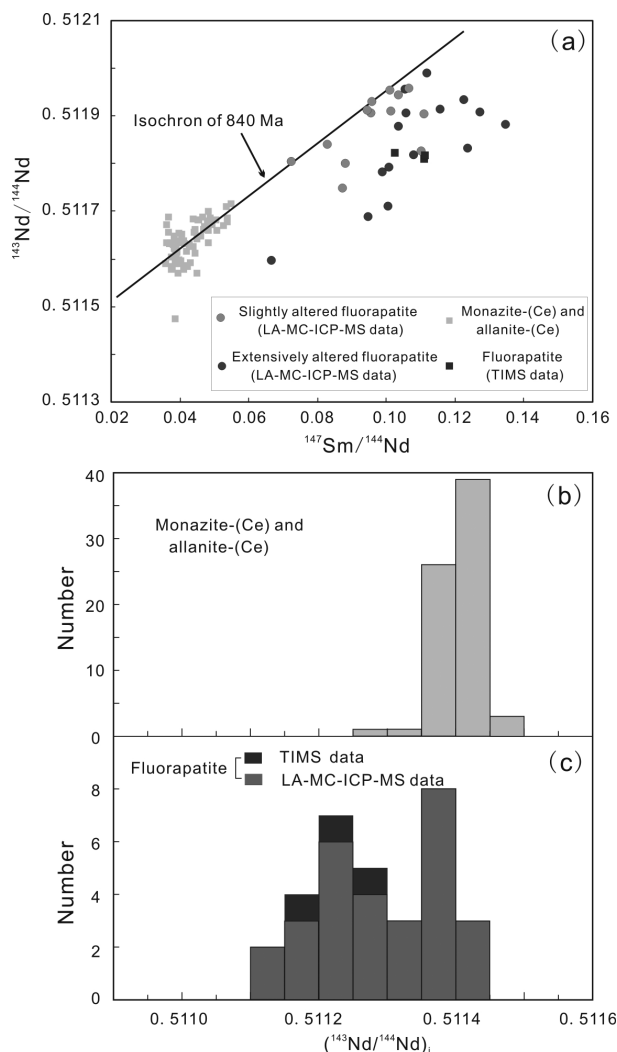
FIGURE 6. (**a**) Plot of $^{143}Nd/^{144}Nd$ vs. $^{147}Sm/^{144}Nd$ for fluorapatite, allanite-(Ce), and monazite-(Ce). A Sm-Nd isochron of 840 Ma is shown for reference. (**b**) Histogram showing initial $^{143}Nd/^{144}Nd$ ratios of allanite-(Ce) and monazite-(Ce). (**c**) Histogram showing initial $^{143}Nd/^{144}Nd$ ratios of fluorapatite.

FIGURE 7. $^{147}Sm/^{144}Nd$ vs. $^{143}Nd/^{144}Nd$ diagrams illustrating: (**a** and **b**) the effect of the Sm/Nd ratio change on the evolution of the Sm-Nd isotopic system, (**c**) methodology regarding the back tracing of the initial isotopic composition of a sample that has experienced a Sm/Nd ratio change, and (**d**) how to back trace the initial isotopic composition of a sample if the change in the Sm/Nd ratio is ignored. See the text for further discussion.

their present-day compositions, together with those of unaltered domains, would still lie on the 840 Ma isochron (Fig. 7a). If the Sm/Nd ratios increased at some later time, the compositional evolutionary paths of the altered domains would be more complex, as graphically illustrated in the $^{147}Sm/^{144}Nd$ vs. $^{143}Nd/^{144}Nd$ diagram (Fig. 7b). At t_0, the initial composition of an unaltered fluorapatite crystal could have been located at Point b_0. As time passed, its composition would have evolved along path b_0-b_1. If the crystal was altered at t_1, its Sm/Nd ratio could have been increased to Point b_1'. From then on, the composition of the altered fluorapatite would evolve along a new path, but the question is where the new path would stop. To help answer this question, we have inserted point d_1 on the reference isochron with an age of (t_0-t_1). This point has the same $^{147}Sm/^{144}Nd$ ratio as Point b_1', but its $^{143}Nd/^{144}Nd$ ratio is higher. Assuming that the Sm-Nd isotopic system of Point d_1 remained closed since t_1, the composition of
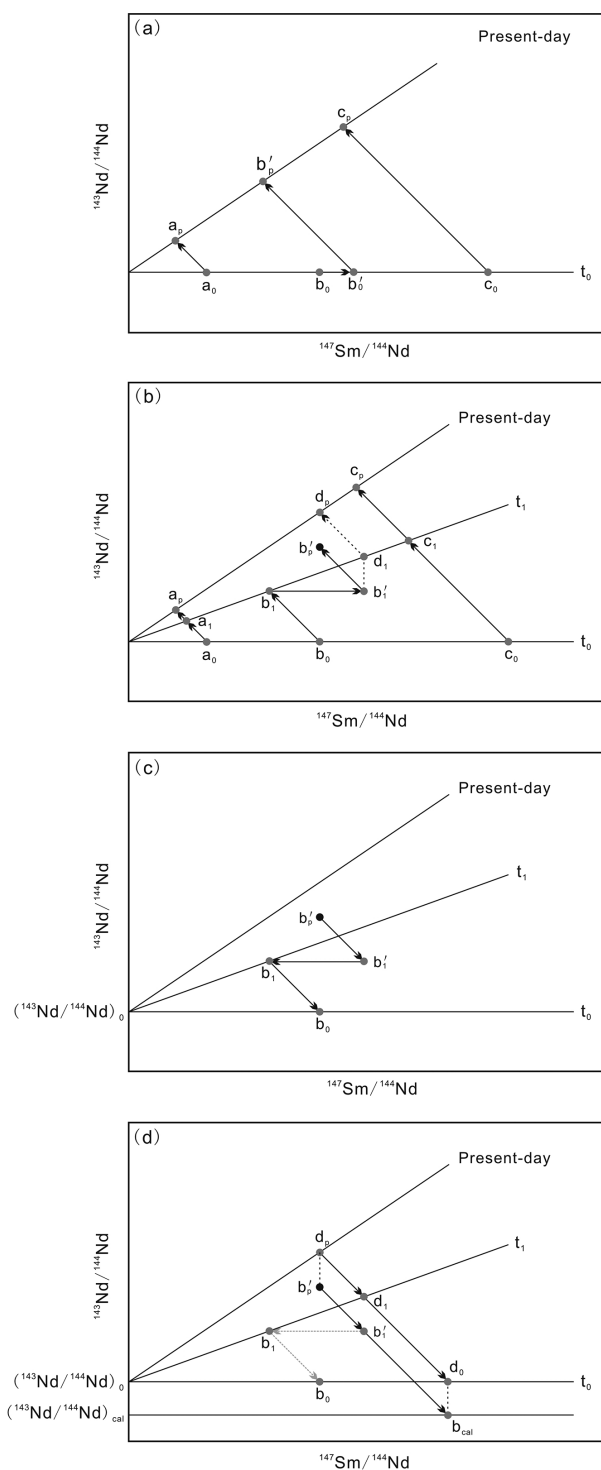
this point would just intersect with the reference isochron of 840 Ma at the present day (Point d_p). Because Points b'_1 and d_1 have the same $^{147}Sm/^{144}Nd$ ratio, the increases in the $^{143}Nd/^{144}Nd$ ratio at the time interval of t_1 to the present day should be the same for the two points. Since Point b'_1 has a $^{143}Nd/^{144}Nd$ ratio lower than that of Point d_1, the path b'_1-b'_p cannot intersect with the isochron of 840 Ma, i.e., the present-day composition of the altered fluorapatite must be plotted below the 840 Ma isochron.

To obtain the initial $^{143}Nd/^{144}Nd$ ratio of the altered fluorapatite, two evolution paths need to be traced backward (Fig. 7c). To obtain the $^{143}Nd/^{144}Nd$ ratio at t_1, path b_p'-b'_1 needs to be traced backward. The mathematical equation can be expressed as:

$$(^{143}Nd/^{144}Nd)_{t1} = (^{143}Nd/^{144}Nd)_p - (^{147}Sm/^{144}Nd)_p(e^{\lambda t1} - 1) \quad (1)$$

where $(^{143}Nd/^{144}Nd)_p$ denotes the present-day $^{143}Nd/^{144}Nd$ ratio, $(^{147}Sm/^{144}Nd)_p$ denotes the present-day $^{147}Sm/^{144}Nd$ ratio, and λ is the decay constant of ^{147}Sm.

To further obtain the $^{143}Nd/^{144}Nd$ ratio at t_0, path b_1-b_0 also needs to be traced backward using the mathematical expression:

$$(^{143}Nd/^{144}Nd)_{t0} = (^{143}Nd/^{144}Nd)_{t1} - (^{147}Sm/^{144}Nd)_{unchanged}(e^{\lambda(t0-t1)} - 1) \quad (2)$$

where $(^{147}Sm/^{144}Nd)_{unchanged}$ denotes the $^{147}Sm/^{144}Nd$ ratio before the metasomatic alteration at t_1.

Substitute Equation 1 into Equation 2:

$$(^{143}Nd/^{144}Nd)_{t0} = (^{143}Nd/^{144}Nd)_p - (^{147}Sm/^{144}Nd)_p(e^{\lambda t1} - 1) - {}^{147}Sm/^{144}Nd)_{unchanged} \cdot [e^{\lambda(t0-t1)} - 1]. \quad (3)$$

The initial $^{143}Nd/^{144}Nd$ ratio of the altered apatite can be obtained.

If the alteration-induced change of the $^{147}Sm/^{144}Nd$ ratio is ignored, one evolutionary path (b'_p-b_{cal}) or two continuous evolutionary paths (b'_p-b'_1 and b'_1-b_{cal}) need to be traced backward (Fig. 7d). The mathematical expression is:

$$(^{143}Nd/^{144}Nd)_{cal} = (^{143}Nd/^{144}Nd)_p - (^{147}Sm/^{144}Nd)_p(e^{\lambda * t1} - 1) - {}^{147}Sm/^{144}Nd)_{unchanged} * [e^{\lambda(t0-t1)} - 1] \quad (4)$$

where $(^{147}Sm/^{144}Nd)_{changed}$ denotes the $^{147}Sm/^{144}Nd$ ratio after the metasomatic alteration at t_1.

It is obvious that the ratio obtained from Equation 4 will be smaller than that obtained from Equation 3, because $(^{147}Sm/^{144}Nd)_{changed}$ is larger than $(^{147}Sm/^{144}Nd)_{unchanged}$.

The above illustrations demonstrate that an increase in the Sm/Nd ratio can cause the present-day composition of the altered apatite to plot below the present-day Sm-Nd isochron, and can also cause the calculated initial $^{143}Nd/^{144}Nd$ ratio to be lower than the actual initial isotopic ratio. Here we want to point out that fluorapatite from the Sin Quyen deposit may have experienced multiple stages of metasomatic alteration, during which the Sm/Nd ratios may have been increased and/or even decreased several times. Thus, here we present only a simple and ideal illustration of the change in the Sm-Nd isotope system. It is also notable that, although the increase(s) in the Sm/Nd ratios can explain the observed Sm-Nd isotopic disturbances, it does not mean that this is the only possible cause. Addition of Nd from compositionally different fluids might also induce somewhat

changes in $^{143}Nd/^{144}Nd$ ratios, and more studies are needed to test this possibility.

IMPLICATIONS

Previous experimental studies have demonstrated that apatite can be altered by a variety of fluids, including aqueous brines ($NaCl$-KCl-$CaCl_2$-H_2O), H_2O-CO_2 aqueous fluids, and low-pH acidic fluids, over a wide range of temperatures (300–900 °C) and pressures (500–1000 MPa) (Harlov et al. 2002b, 2005; Harlov and Förster 2003). In addition to laboratory experiments, apatite from a wide range of natural rocks has also been found to experience metasomatic alteration (Harlov 2015 and references therein). Previous studies concerned mainly on the elemental changes during metasomatic alteration of apatite (e.g., Harlov et al. 2002a; Bonyadi et al. 2011; Li and Zhou 2015; Heidarian et al. 2018), but much less on the alteration-induced Sm-Nd isotopic disturbance.

It has long been assumed that Sm and Nd have very similar chemical behaviors, and thus the Sm/Nd ratios are little affected by hydrothermal alteration (White 2014). However, this study demonstrates that Sm/Nd ratios can obviously be changed during metasomatic alteration, and that this change will affect the evolution of the Sm-Nd isotopic system. Similar results have also been documented in other studies. For example, apatite crystals from magnetite-apatite ores in the Kiruna area, Sweden, also experienced metasomatic alteration, and the alteration induced variable REE removal (Harlov et al. 2002a). The unaltered REE-rich apatite domains have an average Sm/Nd ratio of 0.16, whereas the altered REE-poor domains have an average ratio of 0.21. Similarly, unaltered REE-rich apatite crystals from magnetite ores in the Bafq District, Iran, have Sm/Nd ratios ranging from 0.13 to 0.22, whereas altered REE-poor crystals have ratios ranging from 0.18 to 0.55 (Stosch et al. 2011). It has also been found that unaltered REE-rich fluorapatite domains, from the Yinachang Fe-Cu-(LREE) deposit, southwestern China, have Sm/Nd ratios ranging from 0.14 to 0.25, whereas altered REE-poor domains have ratios ranging from 0.19 to 0.45 (Li and Zhou 2015). These examples indicate that REE loss is a common process during metasomatic alteration of apatite, and the removal of Sm is usually less than the removal of Nd, resulting in an increase in the Sm/Nd ratio. This less removal of Sm may be partially related to its higher compatibility in the apatite structure, as demonstrated in previous apatite-melt REE partition experiments (Watson and Green 1981; Klemme and Dalpe 2003; Prowatke and Klemme 2006). It is also notable that experimental studies demonstrate that, at elevated temperatures (>150 °C), $NdCl^{2+}$ and NdF^{2+} species in hydrothermal solutions are more stable than $SmCl^{2+}$ and SmF^{2+} species, respectively (Migdisov et al. 2009). Because Cl and F are two major anion ligands in most upper crustal fluids (Yardley 2012), the removal of smaller amounts of Sm relative to Nd may also be related to the predominance of Cl^- and/or F^- in the metasomatic fluids.

In addition to the Sm-Nd isotopic system, it has been documented that Sr and O isotopes of apatite can also be modified during metasomatic alteration. For example, the unaltered fluorapatite crystals from the Taocun iron-oxide apatite deposit, eastern China, have $^{87}Sr/^{86}Sr$ ratios ranging from 0.7077 to 0.7087, and $\delta^{18}O$ values ranging from +5.3 to +7.5‰. After reacting with upper crustal meteoric water, the fluorapatite crystals have obviously higher

$^{87}Sr/^{86}Sr$ ratios (0.7083–0.7097) and lower $\delta^{18}O$ values (–3.0 to +3.4‰) (Zeng et al. 2016).

In summary, if metasomatism occurs, bulk-rock isotopic compositions of apatite/apatite-rich rocks may show mixed signatures, and hence be geologically misleading. Therefore, it is important to evaluate the effects of metasomatic alteration on mineral textures and mineral chemistry before using apatite as a geological indicator.

REFERENCES CITED

Bea, F. (1996) Residence of REE, Y, Th, and U in granites and crustal protoliths: Implications for the chemistry of crustal melts. Journal of Petrology, 37, 521–552.

Bonyadi, Z., Davidson, G.J., Mehrabi, B., Meffre S., and Ghazban, F. (2011) Significance of apatite REE depletion and monazite inclusions in the brecciated Se–Chahun iron oxide–apatite deposit, Bafq district, Iran: Insights from paragenesis and geochemistry. Chemical Geology, 281, 253–269.

Chakhmouradian, A.R., Reguir, E.P., Zaitsev, A.N., Coueslan, C., Xu, C., Kynicky, J., Mumin, A.H., and Yang, P. (2017) Apatite in carbonatitic rocks: Compositional variation, zoning, element partitioning and petrogenetic significance. Lithos, 274-275, 188–213.

Fisher, C.M., McFarlane, C.R.M., Hanchar, J.M., Schmitz, M.D., Sylvester, P.J., Lam, R., and Longerich, H.P. (2011) Sm-Nd isotope systematics by laser ablation-multicollector-inductively coupled plasma mass spectrometry: Methods and potential natural and synthetic reference materials. Chemical Geology, 284, 1–20.

Foster, G.L., and Carter, A. (2007) Insights into the patterns and locations of erosion in the Himalaya—A combined fission-track and in situ Sm-Nd isotopic study of detrital apatite. Earth and Planetary Science Letters, 257, 407–418.

Goldoff, B., Webster, J.D., and Harlov, D.E. (2012) Characterization of fluor-chlorapatites by electron probe microanalysis with a focus on time-dependent intensity variation of halogens. American Mieneralogist, 97, 1103–1115.

Hammerli, J., Kemp, A.I.S., and Spandler, C. (2014) Neodymium isotope equilibration during crustal metamorphism revealed by in situ microanalysis of REE-rich accessory minerals. Earth and Planetary Science Letters, 392, 133–142.

Harlov, D.E. (2015) Apatite: a fingerprint for metasomatic processses. Elements, 11, 171–176.

Harlov, D.E., and Förster, H.J. (2002) High-grade fluid metasomatism on both a local and regional scale: the Seward Peninsula, Alaska and the Val Strona di Omegna, Ivrea-Verbano zone, northern Italy. Part II: Phosphate mineral chemistry. Journal of Petrology, 43, 801–824.

——— (2003) Fluid-induced nucleation of REE phosphate minerals in apatite: nature and experiment. Part II. Fluorapatite. American Mineralogist, 88, 1209–1229.

Harlov, D.E., Andersson, U.B., Förster, H.J., Nyström, J.O., Dulski, P., and Broman, C. (2002a) Apatite-monazite relations in the Kiirunavaara magnetite-apatite ore, northern Sweden. Chemical Geology, 191, 47–72.

Harlov, D.E., Förster, H.J., and Nijland, T.G. (2002b) Fluid-induced nucleation of REE-phosphate minerals in apatite: nature and experiment. Part I. Chlorapatite. American Mineralogist, 87, 245–261.

Harlov, D.E., Wirth, R., and Förster, H.J. (2005) An experimental study of dissolution-reprecipitation in fluorapatite: fluid infiltration and the formation of monazite. Contributions to Mineralogy and Petrology, 150, 268–286.

Heidarian, H., Lentz, D.R., Alirezaei, S., McFarlane, C.R.M., and Peighambari, S. (2018) Multiple stage ore formation in the Chadormalu Iron Deposit, Bafq Metallogenic Province, Central Iran: Evidence from BSE imaging and apatite EPMA and LA-ICP-MS U-Pb geochronology. Minerals, 8, 87.

Henderson, A.L., Foster, G.L., and Najman, Y. (2010) Testing the application of in situ Sm-Nd isotopic analysis on detrital apatites: A provenance tool for constraining the timing of India-Eurasia collision. Earth and Planetary Science Letters, 297, 42–49.

Hughes, J.M., and Rakovan, J.F. (2015) Structurally robust, chemically diverse: apatite and apatite supergroup minerals. Elements, 11, 165–170.

Janots, E., Austrheim, H., Spandler, C., Hammerli, J., Trepmann, C.A., Berndt, J., Magnin, V., and Kemp, A. (2018) Rare earth elements and Sm-Nd isotope redistribution in apatite and accessory minerals in retrogressed lower crust material (Bergen Arcs, Norway). Chemical Geology, 484, 120–135.

Jochum, K.P., Nohl, U., Herwig, K., Lammel, E., Stoll, B., and Hofmann, A.W. (2005) GeoReM: A new geochemical database for reference materials and isotopic standards. Geostandards and Geoanalytical Research, 29, 333–338.

Klemme, S., and Dalpe, C. (2003) Trace-element partitioning between apatite and carbonatite melt. American Mineralogist, 88, 639–646.

Li, X.C., and Zhou, M.F. (2015) Multiple stages of hydrothermal REE remobilization recorded in fluorapatite in the Paleoproterozoic Yinachang Fe-Cu-(REE) deposit, Southwest China. Geochimica et Cosmochimica Acta, 166, 53–73.

——— (2017) Hydrothermal alteration of monazite-(Ce) and chevkinite-(Ce) from the Sin Quyen Fe-Cu-LREE-Au deposit, northwestern Vietnam. American Mineralogist, 102, 1525–1541.

Li, X.C., Zhao, J.H., Zhou, M.F., Gao, J.F., Sun, W.H., and Tran, M.D. (2018a) Neoproterozoic granitoids from the Phan Si Pan belt, Northwest Vietnam: Implication for the tectonic linkage between Northwest Vietnam and the Yangtze Block. Precambrian Research, 209, 212–230.

Li, X.C., Zhou, M.F., Chen, W.T., Zhao, X.F., and Tran, M.D. (2018b) Uranium-lead dating of hydrothermal zircon and monazite from the Sin Quyen Fe-Cu-REE-Au-(U) deposit, northwestern Vietnam. Mineralium Deposita, 53, 399–416.

Liu, Z.C., Wu, F.Y., Yang, Y.H., Yang, J.H., and Wilde, S.A. (2012) Neodymium isotopic compositions of the standard monazites used in U-Th-Pb geochronology. Chemical Geology, 334, 221–239.

McLean, R.N. (2001) The Sin Quyen iron oxide-copper-gold-rare earth oxide mineralization of North Vietnam. In T.M. Porter, Ed., Hydrothermal Iron Oxide Copper–Gold & Related Deposits: A Global Perspective, vol. 2, p. 293–301. PGC Publishing, Adelaide.

Migdisov, A.A., Williams-Jones, A.E., and Wagner, T. (2009) An experimental study of the solubility and speciation of the Rare Earth Elements (III) in fluoride- and chloride-bearing aqueous solutions at temperatures up to 300°C. Geochimica et Cosmochimica Acta, 73, 7087–7109.

Pan, Y., and Fleet, M.E. (2002) Composition of the apatite-group minerals: substitution mechanisms and controlling factors. In M.J. Kohn, J. Rakovan, and J.M. Hughes, Eds., Phosphates: Geochemical, Geobiological, and Materials Importance, 48, p. 13–49. Reviews in Mineralogy and Geochemistry, Mineralogical Society of America, Chantilly, Virginia.

Prowatke, S., and Klemme, S. (2006) Trace element partitioning between apatite and silicate melts. Geochimica et Cosmochimica Acta, 70, 4513–4527.

Roeder, P.L., MacArthur, D., Ma, X.P., Palmer, G.R., and Mariano, A.N. (1987) Cathodoluminescence and microprobe study of rare-earth elements in apatite. American Mineralogist, 72, 801–811.

Schoneveld, L., Spandler, C., and Hussey, K. (2015) Genesis of the central zone of the Nolans Bore rare earth element deposit, Northern Territory, Australia. Contributions to Mineralogy and Petrology, 170, 11.

Stosch, H.G., Romer, R.L., Daliran, F., and Rhede, D. (2011) Uranium-lead ages of apatite from iron oxide ores of the Bafq District, East-Central Iran. Mineralium Deposita, 46, 9–21.

Ta, V.D. et al. (1975) The geological report on detailed exploration of the Sin Quyen copper deposit. General Department of Geology, Hanoi (unpublished).

Watson, E.B., and Green, T.H. (1981) Apatite/liquid partition coefficients for the rare-earth elements and strontium. Earth and Planetary Science Letters, 56, 405–421.

White, W.M. (2014) Isotope Geochemistry, 498 p. Wiley.

Wu, F.Y., Yang, Y.H., Li, Q.L. Mitchell, R.H., Dawson, J.B., Brandl, G., and Yuhara, M. (2011) In-situ determination of U–Pb ages and Sr–Nd–Hf isotopic constraints on the petrogenesis of the Phalaborwa carbonatite Complex, South Africa. Lithos, 127, 309–322.

Wu, F.Y., Arzamastsev, A.A., Mitchell, R.H., Li, Q.L., Sun, J., Yang, Y.H., and Wang, R.C. (2013) Emplacement age and Sr–Nd isotopic compositions of the Afrikanda alkaline ultramafic complex, Kola Peninsula, Russia. Chemical Geology, 353, 210–229.

Yang, Y.H., Wu, F.Y., Yang, J.H., Chew, D.M., Xie, L.W., Chu, Z.Y., Zhang, Y.B., and Huang, C. (2014) Sr and Nd isotopic compositions of apatite reference materials used in U-Th-Pb geochronology. Chemical Geology, 385, 35–55.

Yardley, B.W.D. (2012) The chemical composition of metasomatic fluids in the crust. In D.E. Harlov and H. Austrheim, Eds., Metasomatism and the Chemical Transformation of Rock, p. 17–53. Springer.

Zeng, L.P., Zhao, X.F., Li, X.C., Hu, H., and McFarlane, C. (2016) In situ elemental and isotopic analysis of fluorapatite from the Taocun magnetite-apatite deposit, Eastern China: Constraints on fluid metasomatism. American Mineralogist, 101, 2468–2483.

Endnote:

[1]Deposit item AM-18-96501, Supplemental Material. Deposit items are free to all readers and found on the MSA web site, via the specific issue's Table of Contents (go to http://www.minsocam.org/MSA/AmMin/TOC/2018/Sep2018_data/Sep2018_data.html).